ARL-TR-9235 ● JULY 2021

DEVCOM ARMY RESEARCH LABORATORY

Combining Sparse and Dense Databases to Form a Robust Aerodynamic Model for a Long-Range High-Speed Projectile

by Bradley T Burchett, Joseph D Vasile, and Joshua T Bryson

Approved for public release: distribution unlimited.

NOTICES

Disclaimers

The findings in this report are not to be construed as an official Department of the Army position unless so designated by other authorized documents.

Citation of manufacturer's or trade names does not constitute an official endorsement or approval of the use thereof.

Destroy this report when it is no longer needed. Do not return it to the originator.

ARL-TR-9235 ● JULY 2021



Combining Sparse and Dense Databases to Form a Robust Aerodynamic Model for a Long-Range High-Speed Projectile

Bradley T Burchett, Joseph D Vasile, and Joshua T Bryson
Weapons and Materials Research Directorate,
DEVCOM Army Research Laboratory

Approved for public release: distribution unlimited.

REPORT DOCUMENTATION PAGE

Form Approved
OMB No. 0704-0188

Public reporting burden for this collection of information is estimated to average 1 hour per response, including the time for reviewing instructions, searching existing data sources, gathering and maintaining the data needed, and completing and reviewing the collection information. Send comments regarding this burden estimate or any other aspect of this collection of information, including suggestions for reducing the burden, to Department of Defense, Washington Headquarters Services, Directorate for Information Operations and Reports (0704-0188), 1215 Jefferson Davis Highway, Suite 1204, Arlington, VA 22202-4302. Respondents should be aware that notwithstanding any other provision of law, no person shall be subject to any penalty for failing to comply with a collection of information if it does not display a currently valid OMB control number.
PLEASE DO NOT RETURN YOUR FORM TO THE ABOVE ADDRESS.

1. REPORT DATE *(DD-MM-YYYY)*	2. REPORT TYPE	3. DATES COVERED (From - To)
July 2021	Technical Report	1 November 2020–14 May 2021

4. TITLE AND SUBTITLE
Combining Sparse and Dense Databases to Form a Robust Aerodynamic Model for a Long-Range High-Speed Projectile

5a. CONTRACT NUMBER

5b. GRANT NUMBER

5c. PROGRAM ELEMENT NUMBER

6. AUTHOR(S)
Bradley T Burchett, Joseph D Vasile, and Joshua Bryson

5d. PROJECT NUMBER

5e. TASK NUMBER

5f. WORK UNIT NUMBER

7. PERFORMING ORGANIZATION NAME(S) AND ADDRESS(ES)
DEVCOM Army Research Laboratory
ATTN: FCDD- RLW-WD
Aberdeen Proving Ground, MD 21005

8. PERFORMING ORGANIZATION REPORT NUMBER
ARL-TR-9235

9. SPONSORING/MONITORING AGENCY NAME(S) AND ADDRESS(ES)

10. SPONSOR/MONITOR'S ACRONYM(S)

11. SPONSOR/MONITOR'S REPORT NUMBER(S)

12. DISTRIBUTION/AVAILABILITY STATEMENT
Approved for public release: distribution unlimited.

13. SUPPLEMENTARY NOTES
ORCID IDs: Bradley T Burchett, 0000-0002-1934-0537; Joshua Bryson, 0000-0002-0753-6823; Joseph D Vasile, 0000-0003-3812-6277

14. ABSTRACT
Several aerodynamic databases are combined to form an aerodynamic model for a high-speed long-range missile. A large test matrix of flight conditions was formed and exercised on a semi-empirical prediction code and an inviscid computation fluid dynamics (CFD) solver, providing full-density databases of low fidelity. Higher-fidelity methods, specifically Navier–Stokes CFD and wind tunnel tests, were applied to a small subset of the test matrix resulting in sparse but accurate predictions of the aerodynamic forces and moments. In this work we demonstrate a novel approach to combining the databases such that features of the low-fidelity predictions are preserved as they are tuned to intersect the sparse data provided by the high-fidelity sources. This is done by modeling the dense predictions with a set of basis functions, then tuning the basis functions to intersect the points from the high-fidelity sources. Harmonic basis functions are used to reflect the cyclical symmetry of the projectile used in this study. Examples show that this method outperforms established kriging methods.

15. SUBJECT TERMS
projectile aerodynamics, wind tunnel, WT, computation fluid dynamics, CFD, data fusion

16. SECURITY CLASSIFICATION OF:			17. LIMITATION OF ABSTRACT	18. NUMBER OF PAGES	19a. NAME OF RESPONSIBLE PERSON
a. REPORT	b. ABSTRACT	c. THIS PAGE			Bradley T Burchett
Unclassified	Unclassified	Unclassified	UU	35	19b. TELEPHONE NUMBER (Include area code) (410) 306-0792

Standard Form 298 (Rev. 8/98)
Prescribed by ANSI Std. Z39.18

Contents

List of Figures iv

List of Tables iv

1. Introduction 1

2. Data Sources 2

3. Method: Fourier Series Interpolation and Superposition 6

3.1 The Complex Valued Fourier Series 6

3.2 Collecting Smoothed CFD Predictions for a Range of AOA 7

3.3 Full Model Buildup by Superposition 8

4. Tuning the Basis Functions 9

4.1 RAS Components 9

4.2 MAS Components 12

5. Polynomial Regression and Build 18

6. Results 18

7. Conclusion 25

8. References 26

List of Symbols, Abbreviations, and Acronyms 27

Distribution List 29

List of Figures

Fig. 1 High-speed LTV-1 2

Fig. 2 Sparsity pattern of the CFD++ computational test matrix for pitch moment, entire airframe, Mach = 0.75, and zero deflections 4

Fig. 3 Sparsity pattern of the WT data for pitch moment after interpolation and replication, entire airframe, Mach = 2, and zero deflections 5

Fig. 4 RASs, side-force CFD data at Mach 2 (dots). Fourier interpolation is superimposed (solid lines) showing smoothing, symmetry, and null points at phi-0°, 45°,… 360°..... 7

Fig. 5 RASs, side-force CFD data at Mach 2, and Fourier approximations from Fig. 4 collected in a single surface 8

Fig. 6 Viewing the aero buildup as a network with tuning applied to the RAS terms..... 9

Fig. 7 Sequence of iterates for RAS tuning, pitch moment, Mach = 0.75, AOA = 6°. The blue curve is the Cart3D data manifold for the built-up coefficient before tuning, and diamonds depict the CFD++ data available. X's are the iterates that become brighter red for subsequent iterations..... 12

Fig. 8 Tuning MAS terms by backpropagation..... 14

Fig. 9 Pitch coefficient matching prior to and after network tuning, Mach = 2.0..... 17

Fig. 10 Side-moment coefficient comparison for all data sources, plus mode, Mach = 2.0, roll angle = 22.5° 20

Fig. 11 Pitch coefficient comparison for all data sources, Mach = 2.0, roll angle = 0° 22

Fig. 12 Side-force coefficient comparison for all data sources, plus mode, Mach = 2.0, roll angle 22.5° 23

Fig. 13 Normal force coefficient comparison for all data sources, plus mode, Mach = 2.0, roll angle = 22.5° 24

List of Tables

Table 1 Wind tunnel test conditions (courtesy of Florida State University) 5

1. Introduction

As computational fluid dynamics (CFD) software packages become ubiquitous in aerospace applications, and computing power continues to become more affordable, researchers can produce large sets of aerodynamic predictions at the touch of a button.[1–3] The accuracy of these predictions is typically proportional to the number of floating point operations expended in computing each prediction. That quantity is a function of the grid size and prediction method (inviscid, Reynolds-averaged Navier–Stokes [RANS], large-eddy simulation, etc.). Thus, due to constraints of cost and time, it is customary to render large tables of predictions using less-accurate methods, while more-precise predictions are limited to coarse tables. When experiments such as wind tunnel (WT) tests are added to the mix, the experimental table is likely to be even more sparse than the most precise CFD predictions. In essence, if an engineer is dealing with multiple "data" sources, those less costly solutions are likely to provide more-comprehensive tables in Mach, angle of attack (AoA), roll, and deflections. The more accurate and more costly sources will provide fewer table entries; however, their predictions should be trusted as closer to the truth.

This situation arises in many disciplines since more-accurate instrumentation typically comes with a higher cost, lower bandwith, and lower duty cycle. A brief review of the literature on aerodynamic data fusion from multifidelity sources reveals that most techniques involve the use of "surrogate models" that can take many forms.[4–6] The surrogate model is used in place of the highest-fidelity models to allow for repeated low-cost predictions during the tuning process. Some surrogate models are physics-based equations typically of reduced order. Many are simply basis functions without any grounding in the underlying physics. In this work we use a surrogate model based upon Fourier series we have outlined in an accompanying report.[7]

In this work we tune a Fourier model to the WT data using an approach from linear feedforward neural networks. The method is demonstrated on computational predictions and experimental observations from the Laboratory Technology Vehicle (LTV), a long-range high-speed projectile. Figure 1 depicts the CAD model of LTV-1. It is designed for high-speed long-range flight with four long low-aspect-ratio fins to enhance body lift at non-zero AoAs. Due to these lifting surfaces, the aerodynamic forces and moments are strongly roll-dependent. In this work, all of the data sources were given in the wind or "tunnel" frame, unlike the previous work where we modeled them in the body frame. Thus forces and moments are measured much like they would be in a WT: The model is rotated with respect to the flow; however, the forces and moments are measured in a frame fixed to the tunnel.

Figure 1b depicts a projection of the relative wind and aerodynamic roll angle. The wind frame unit vectors for transverse forces $\{\hat{S}, \hat{N}\}$ and moments $\{\hat{m}, \hat{n}\}$ are depicted extending from the projectile axis of symmetry. The body frame unit vectors for normal and side force are depicted at the right edge of the figure for contrast.

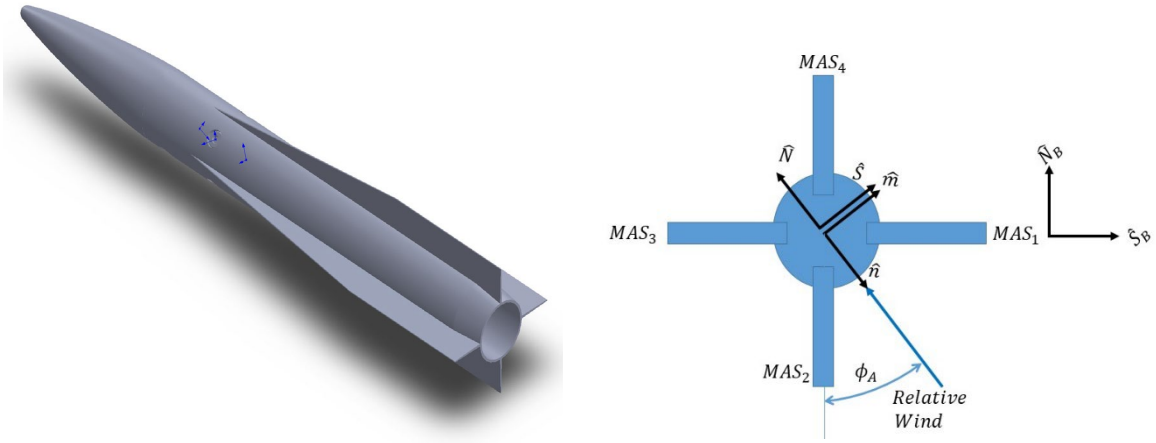

a) Isometric view of 3-D model **b) Tail view in "plus" mode; aerodynamic roll and local frames defined**

Fig. 1 High-speed LTV-1

We conclude this report by comparing the final model to the data sources to show model evolution, averaging, and accuracy. An alternative model is formed based on the kriging method from Ghoreyshi et al.[4] Selected comparisons show that our method matches the training data, expected symmetry, and null points better than the kriging method.

2. Data Sources

To provide high-fidelity predictions within a 6 degrees of freedom (6DOF) simulation, several methods of increasing accuracy were used to estimate the aerodynamic forces and moments for the LTV-1 projectile: the DATCOM semi-empirical aero-prediction code, NASA's Cart3D Euler Computation Fluid Dynamic code (C3D), Metacomp's CFD++ RANS simulation, and a WT experiment performed at Florida State University.[8]

Since the aerodynamic forces and moments for this airframe tend to be highly roll- dependent, a dense matrix of test points was determined for the lower-fidelity methods. Each force/moment is dependent upon Mach number (M), AoA (α), aerodynamic roll angle (ϕ), and for moveable aerodynamic surface (MAS) terms,

flap deflection (δ). The full test matrix can be described as all possible combinations of the following:

$$M \in \{0.45, 0.55, 0.65, 0.75, 0.85, 0.95, 1.02, 1.2, 1.5, 2, 2.5, 3, 3.5, 4, 6, 9\}, N_M = 16$$

$$\phi \in \{0°, 11.25°, 22.5°, \ldots 348.75°\}, N_\phi = 32$$

$$\alpha \in \{0°, 2°, 4°, \ldots, 20°, 25°\}, N_\alpha = 12$$

$$\delta \in \{-30°, -25°, \ldots -5°, -2°, 0°, 2°, 5°, 10°, \ldots, 30°\}, N_\delta = 15$$

Thus the total number of cases computed in DATCOM and Cart3D is

$$N_M \cdot N_\phi \cdot N_\alpha \cdot N_\delta = 92160.$$

Cart3D was used to predict the force and moment vectors for the rigid aero surfaces (R, RASs) and MASs (M) separately ($C_\vartheta^R, C_\vartheta^M\ \vartheta \in \{A, S, N, l, m, n\}$) as well as the total for the entire airframe (C_ϑ^B). Cart3D also calculated the MAS hinge moments. These results were stored in 12 × 16 × 33 arrays ($\alpha \times M \times \phi$) for RAS and sets of 12 × 16 × 33 arrays—one for each δ—for MAS. Data for 0° bank were replicated to create the 33rd layer for 360° bank.

DATCOM was used to predict the force and moment vectors for the entire airframe. Its output was stored in 12 × 16 × 33 arrays to correspond pointwise to the Cart3D results. The DATCOM drag data were used to directly replace Cart3D drag. This is done by finding a Fourier basis fit to DATCOM drag (Section 3) and using it in place of Cart3D. The other DATCOM predictions are ignored.

High-fidelity methods are computationally expensive and could not fill the entire test matrix without incurring a prohibitive computational cost. CFD++ was used to predict a subset of the total force and moment components for the entire airframe at points described by

$$M \in \{0.65, 0.75, 0.85, 0.95, 1.02, 1.2, 1.5, 2, 2.5, 3, 3.5, 4\}, N_M = 12$$

$$\alpha \in \{0°, 2°, 4°, \ldots, 12°\}, N_\alpha = 7$$

$$\phi \in \{0°, 11.25°, 22.5°, \ldots 78.75°\}, N_\phi = 8$$

$$\delta = 0°$$

These data were stored in 12 × 16 × 33 arrays to correspond pointwise to the Cart3D results. These arrays were filled with NaNs (not a number) where computation in CFD++ was skipped. Figure 2 illustrates the points actually computed in CFD++ as blue dots where rows are points in α, and columns are points in ϕ from the Cart3D test grid for pitch moment at Mach 0.75. The axis scaling is by indices into the array rather than the independent variables.

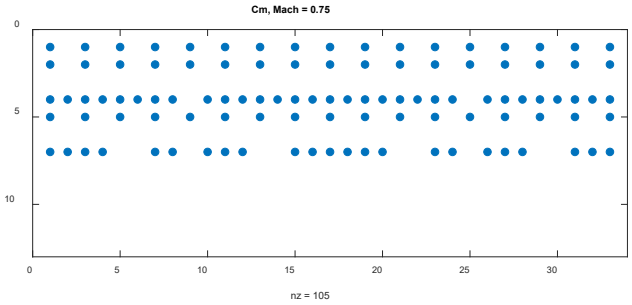

Fig. 2 Sparsity pattern of the CFD++ computational test matrix for pitch moment, entire airframe, Mach = 0.75, and zero deflections

Since these were was for zero deflections, symmetry was invoked so that the computational output was replicated each 90° of bank.

A large set of data was collected using a 1/5 scale model at the Florida State University WT.[8] Test conditions are described in Table 1. Even though this is an extensive test set for the WT, these data are still sparse in comparison with that of the low-fidelity computational methods. Also note that due to the experimental nature of these tests, the points in the Cart3D test grid were not duplicated exactly. Because of this, the WT data were interpolated across Mach, α, and ϕ to the Cart3D input table, and these results were stored in 12 × 16 × 33 arrays. Extrapolation was avoided and no data were available for $\alpha > 12$ or $M > 4$. Since roll sweeps were performed at $\alpha \in \{0°, 6°, 12°\}$, and α sweeps were performed for $\phi \in \{0°, 45°\}$, symmetry could be invoked (replicating the results each 90° of bank) to produce the sparsity pattern shown in Fig. 3 for all Mach numbers 4 and below. Points that could not be interpolated from adjacent conditions in the WT were filled with NaNs.

Table 1 Wind tunnel test conditions (courtesy of Florida State University)

Model	Deflections	Mach number	Pitch/roll sweeps
Baseline	0	0.4, 0.5, 0.6, 0.8, 0.9, 1.1, 1.2, 5	Pitch: 0° to 12° at Phi = 0° Pitch: 0° to 12° at Phi = 45° Roll: –90° to 90° at Alpha = 12° Roll: –90° to 90° at Alpha = 6°
	0	3, 5	Pitch: 0° to 12° at Phi = 0° Pitch: 0° to 12° at Phi = 45° Roll: –90° to 90° at Alpha = 12° Roll: –90° to 90° at Alpha = 6° Roll: 90° to –90° at Alpha = 0°
	0	2	Roll: –90° to 90° at Alpha = 10° Roll: –90° to 90° at Alpha = 4°
	0	0.7, 2	Pitch: 0° to 12° at Phi = 0° Pitch: 0° to 12° at Phi = 45° Roll: –90° to 90° at Alpha = 12° Roll: –90° to 90° at Alpha = 6° Roll: 90° to –90° at Alpha = 0°
Deflected	+El –El	0.7, 2	Pitch: 0° to 12° at Phi = 0° Pitch: 0° to 12° at Phi = 45°
	+Ail –Ail	0.7, 2	Roll: –90° to 90° at Alpha = 12° Roll: –90° to 90° at Alpha = 6° Roll: 90° to –90° at Alpha = 0°

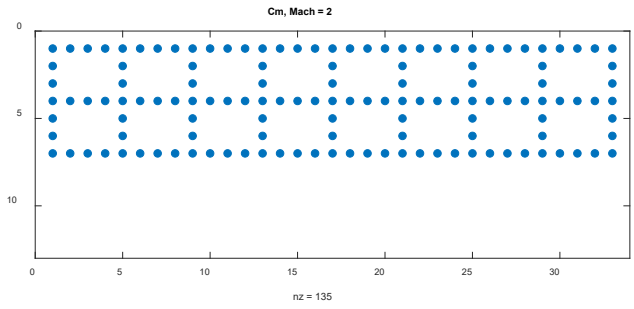

Fig. 3 Sparsity pattern of the WT data for pitch moment after interpolation and replication, entire airframe, Mach = 2, and zero deflections

3. Method: Fourier Series Interpolation and Superposition

Figure 1 depicts the CAD model of the LTV-1, which is designed for high-speed long-range flight with four long strakes to enhance body lift at non-zero AoA. Due to these lifting surfaces, the aerodynamic forces and moments are strongly roll-dependent. In a previous study,[7] we chose to smooth and interpolate CFD force and moment predictions using harmonic basis functions. Since the projectile has periodic symmetry, harmonic basis functions were a logical choice to properly interpret the CFD output along the roll direction. Such basis functions ensured the appropriate symmetry and null points for each of the force and moment terms.

3.1 The Complex Valued Fourier Series

Any periodic function $f(t)$ with period T may be approximated by the finite series of harmonics

$$\hat{y} = X_0 + 2\sum_n |X_n| \cos(2\pi n \cdot \phi/T + \angle X_n) \tag{1}$$

where X_n is a complex number defined by

$$X_n = \frac{1}{T}\int_0^T f(t) e^{-\frac{2\pi n i t}{T}} dt \tag{2}$$

In this work, all of the data sources were given in the wind or "tunnel" frame, unlike the previous work, where we modeled them in the body frame. Thus, forces and moments are measured much like they would be in a WT: The model is rotated with respect to the flow; however, the forces and moments are measured in a frame fixed to the tunnel. Considering the periodic symmetry of the projectile outer mold line, the period is assumed to be $T = \pi/2$ for RASs (body and strakes), and $T = 2\pi$ for MASs since they move independently.

The results of CFD are discrete points representing a force or moment component at a specific Mach number, AoA, and aerodynamic roll. Eq. 2 is applied to each of these, integrating along the roll axis. Due to the discrete nature of the data, trapezoidal integration (trapz) renders an exact solution to Eq. 2 where $f(t)$ is the input data and dt is the discretization (typically 11.25° for the most-dense data sources).

Figure 4 shows the CFD side-force estimates for the rigid aerodynamic surfaces at Mach 2 for a range of AoAs. Some outliers have already been removed and replaced; the methods involved are described in our previous work. The solid lines

are the instances of Eq. 3 found at each AoA by applying Eq. 4 to the data. Note the solid lines provide a smooth interpolation of the data that provides the expected symmetry and null points every 45° of bank. The given "data" exhibits the expected period of $\pi/2$.

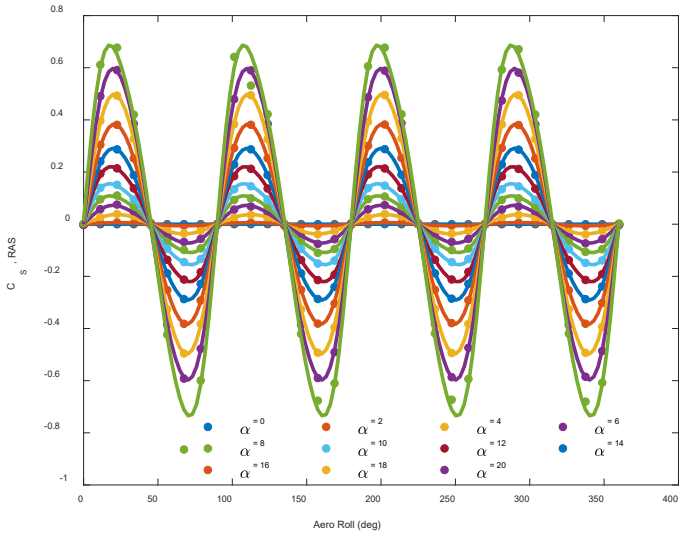

Fig. 4 RASs, side-force CFD data at Mach 2 (dots). Fourier interpolation is superimposed (solid lines) showing smoothing, symmetry, and null points at phi-0°, 45°,… 360°.

3.2 Collecting Smoothed CFD Predictions for a Range of AoA

The end result of our modeling effort will be a set of tables of polynomial coefficients for each of the force and moment components ($C_\vartheta^R, C_\vartheta^M\ \vartheta \in \{A, S, N, l, m, n\}$), where R denotes the rigid aerodynamic surfaces and M denotes the moveable ones. In the "ARL 6DOF" simulation,[1] individual force/moment terms are then predicted by a high-order polynomial in AoA, α, such as

$$C_\vartheta^R = C_{\vartheta 0}^R(M,\phi) + C_{\vartheta 1}^R(M,\phi)s_\alpha + C_{\vartheta 2}^R(M,\phi)s_\alpha^2 + C_{\vartheta 3}^R(M,\phi)s_\alpha^3 + C_{\vartheta 4}^R(M,\phi)s_\alpha^4 + C_{\vartheta 5}^R(M,\phi)s_\alpha^5 \quad (3)$$

where $s_\alpha = \sin\alpha$. Our focus here is assembling and tuning a surface that represents each term $C_\vartheta^R(M,\phi,\alpha)$ and $C_\vartheta^M(M,\phi,\alpha,\delta)$ and provides the highest possible accuracy given the predictions of varying fidelity available. For instance, if we look at $C_\vartheta^R(M,\phi,\alpha)$ for a specific mach number, we can depict the CFD predictions and Fourier models as shown in Fig. 4, or stretching the AoA axis into the page, we can plot a surface as shown in Fig. 5. Our goal is to preserve the shape of this surface while tuning the underlying basis functions to intersect the high-fidelity predictions.

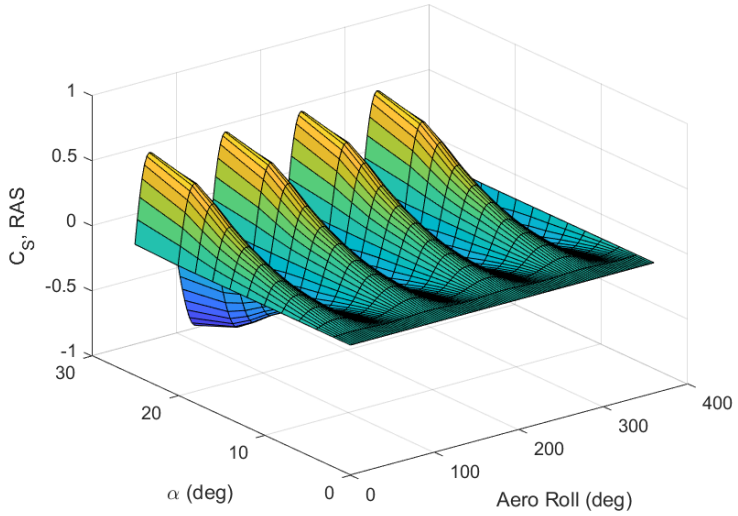

Fig. 5 RASs, side-force CFD data at Mach 2, and Fourier approximations from Fig. 4 collected in a single surface

3.3 Full Model Buildup by Superposition

Since the data sources were all provided in the "wind" or "tunnel" frame, we keep all of our analysis in this frame. One advantage of using this frame is that all components are found in a common frame, so the buildup is accomplished by a simple sum of like components:

$$C_{\vartheta}^{B} = C_{\vartheta}^{R} + C_{\vartheta}^{M_1} + C_{\vartheta}^{M_2} + C_{\vartheta}^{M_3} + C_{\vartheta}^{M_4} \tag{4}$$

This is also convenient since three of the four data sources (DATCOM, CFD++, and WT) only provide predictions for the entire body. However, we want the final model to be decomposed into contributions from the rigid aero surfaces (R) and individual moveable surfaces (M_i) in order to predict maneuvering flight (Fig. 6).

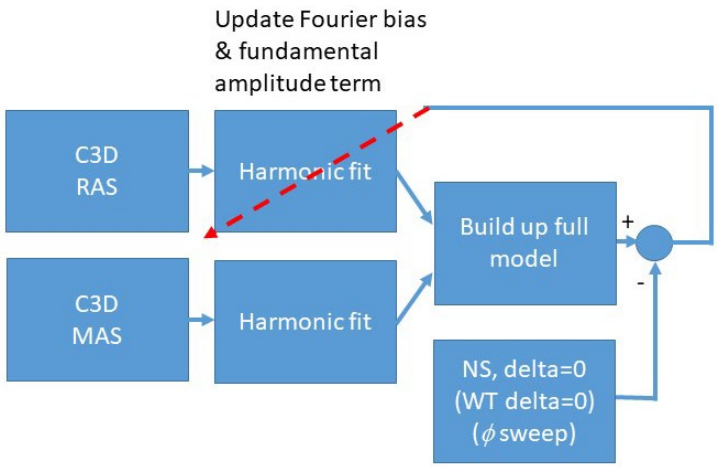

Fig. 6 Viewing the aero buildup as a network with tuning applied to the RAS terms

Note that aerodynamic bank is defined as the angle subtended from the body Z axis (MAS2) counterclockwise to the relative wind. Thus, moving clockwise from MAS1 to MAS2, the aerodynamic bank in the local MAS2 frame is the body aerodynamic bank plus $\pi/2$. Continuing to move around the projectile, the aerodynamic bank angle for each subsequent MAS is $\pi/2$ larger than the previous one. Specifically, this is results in

$$C_{\vartheta}^{M_2}(\phi) = C_{\vartheta}^{M_1}\left(\phi + \frac{\pi}{2}\right), \quad C_{\vartheta}^{M_3}(\phi) = C_{\vartheta}^{M_1}(\phi + \pi), \tag{5a,b}$$

$$C_{\vartheta}^{M_4}(\phi) = C_{\vartheta}^{M_1}(\phi + 3\pi/2) \tag{5c}$$

4. Tuning the Basis Functions

4.1 RAS Components

The Fourier approximations for the RAS force and moment predictions, (C_{ϑ}^{R}) will be modified to intersect the CFD++ and WT data points in turn. Since the more trusted data sources only provide forces and moments for the entire vehicle, the buildup algorithm (Section 3.3) outlined previously will need to be applied to the Fourier of low-fidelity RAS estimates and the MAS1 estimates. For simplicity, we will use data that are all computed in the "wind" frame. Plainly put, this makes Eq. 4 into a simple sum of like components:

$$C_{\vartheta}^{B} = C_{\vartheta}^{R} + C_{\vartheta}^{M_1} + C_{\vartheta}^{M_2} + C_{\vartheta}^{M_3} + C_{\vartheta}^{M_4} \tag{4}$$

Also, note from Eqs. 5a, 5b, and 5c that assembly of the four MAS terms actually pulls data from the same table (à la Fig. 5) at four bank angles. Only the RAS terms will be tuned using the zero deflection data from CFD++ and WT. This makes sense because the MAS terms approximately cancel each other out for transverse forces and moments at zero deflections. This approximation is exact at zero AoA, and loses accuracy with increasing AoA.

If we substitute Fourier for the RAS term into the buildup,

$$C_\vartheta^B(\phi_i, \delta_q) = X_0^R + \sum_n |X_n|_\vartheta^R \cdot \cos(1 \cdot \phi_i + \angle X_n) + \sum_i C_\vartheta^{M_i}(\phi_i) \tag{6}$$

A unique Fourier approximation $\left(X_0^R, |X_n|_\vartheta^R\right)$ was found for each AoA in the test matrix. We choose to tune the bias and fundamental amplitude terms in each approximation at a specific AoA, as follows.

Compute the total prediction using Eq. 6 and compare with the more trusted data source.

$$\mathbf{R}_i = C_\vartheta^B(\phi_i, \delta_q, \alpha) - C_\vartheta^{NS}(\phi_i, \delta_q, \alpha), \qquad \forall\ i \in NS \tag{7}$$

The number of data points *i* at each AoA varies with the data source. A fully dense data source will provide 33 points, one for each bank angle in the test grid. The bias term is corrected immediately by subtracting the mean of the residual

$$X_0^{R+} = X_0^R - \bar{\mathbf{R}} \tag{8}$$

Next, recompute the prediction and residual with the updated bias. Apply a steepest descent algorithm to tune the amplitude of the fundamental frequency, as follows. The sensitivity of the *i*th Fourier predition to the fundamental amplitude ($n = 1$) can be found as

$$\frac{\partial C_\vartheta^B(\phi_i, \delta_q)}{\partial |X_1|_m^R} = \cos(1 \cdot \phi_i + \angle X_1) \tag{9}$$

If we view Eq. 6 as a single-layer linear network, and apply a least-squares criterion,

$$E = \frac{i}{2} \sum_i \left(C_\vartheta^B(\phi_i, \delta_q) - C_\vartheta^{NS}(\phi_i, \delta_q) \right)^2$$

where *i* indicates a training pair and *NS* indicates the Navier–Stokes (CFD++) data, we can write

$$\frac{\partial E}{\partial |X_1|_\vartheta^R} = \frac{\partial E}{\partial C_\vartheta^B(\phi_i, \delta_q)} \cdot \frac{\partial C_\vartheta^B(\phi_i, \delta_q)}{\partial |X_1|_\vartheta^R} \tag{10}$$

where

$$\frac{\partial E}{\partial C_{\vartheta}^{B}(\phi_i, \delta_q)} = \left(C_{\vartheta}^{B}(\phi_i, \delta_q) - C_{\vartheta}^{NS}(\phi_i, \delta_q)\right) = \mathbf{R}_i \tag{11}$$

The total sensitivity of a prediction set for one AoA is then found by summing Eq. 10 for all *i*. Substituing Eq. 9 and Eq. 11, we get

$$\sum_i \frac{\partial E}{\partial |X_1|_{\vartheta}^{R}} = \sum_i \cos(1 \cdot \phi_i + \angle X_1) \cdot \mathbf{R}_i \tag{12}$$

This can be found by an inner product of the phase vector and the residual vector.

After Eq. 8 is applied to correct the bias, the bias is left unchanged and the fundamental frequency is updated repeatedly using Eq. 13, where a learning rate of the reciprocal of the number of elements in the residual vector (λ) is introduced.

$$|X_1|_{\vartheta}^{R} = |X_1|_{\vartheta}^{R+} - 1/\lambda \sum_i \frac{\partial E}{\partial C_{\vartheta}^{B}(\phi_i, \delta_q)} \tag{13}$$

Eq. 13 is applied for 14 iterations (after the bias correction), usually resulting in satisfactory convergence of the Fourier prediction to the more trusted data source.

Figure 7 illustrates the tuning for the RAS pitch moment at Mach = 0.75 and AoA = 6°. CFD++ provides 31 data points for this condition. The blue curve depicts points on the untuned pitch moment manifold at these 31 points before tuning. The first correction is only in bias and moved the predictions to the darkest set of X's. As the fundamental amplitude is gradually adjusted, we depict each subsequent iteration as brighter red X's. After 15 iterations, the 2-norm of the residual vector is reduced from 2.09 to 0.81—a 61% reduction.

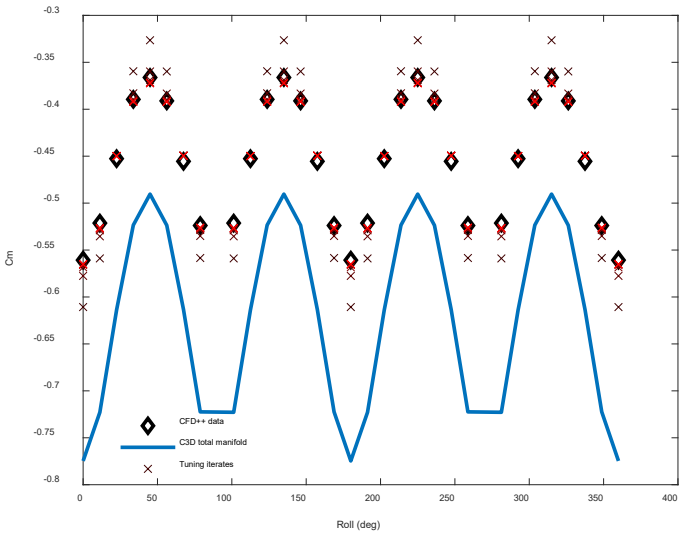

Fig. 7 Sequence of iterates for RAS tuning, pitch moment, Mach = 0.75, AoA = 6°. The blue curve is the Cart3D data manifold for the built-up coefficient before tuning, and diamonds depict the CFD++ data available. X's are the iterates that become brighter red for subsequent iterations.

4.2 MAS Components

Since WT data were available for a variety of "pitch deflected" cases and configurations, albeit in AoA sweeps, we sought to contrive a method to tune the flap control authority in pitch (namely $C_m^{M_i}$). Because we only have AoA sweeps, we effectively have one red stripe from Fig. 5 per flap deflection/configuration and Mach number. That stripe is at 0° of bank for plus configurations and at 45° of bank for X configurations. Referring to Fig. 5, note distinct Fourier approximations were found at each AoA in the test matrix during the interpolation and smoothing step. Thus, we propose an intermediate step, where the Fourier approximation for the MAS $C_m^{M_i}$ is modified to intersect the WT data points. This will be a somewhat involved process, however, since the WT data is for the entire vehicle, while the Fourier fits are for individual (MAS, RAS) components. For simplicity, we will use data that are all computed in the "wind" frame. Plainly put, this makes Eq. 4 a simple sum of like components:

$$C_m^B = C_m^R + C_m^{M_1} + C_m^{M_2} + C_m^{M_3} + C_m^{M_4} \tag{4}$$

Also, note from Eqs. 5a, 5b, and 5c that assembly of the four MAS terms actually pulls data from the same table (à la Fig. 5) at four bank angles. For the pitch configurations, two deflections are used to eliminate roll and yaw tendencies, so ultimately we pull from two or three deflection tables (two flaps are set to zero in the plus configuration). Noting that the deflections are set to

$$[\boldsymbol{\delta_1} \quad \boldsymbol{\delta_2} \quad \boldsymbol{\delta_3} \quad \boldsymbol{\delta_4}] = [\boldsymbol{\delta_q} \quad \mathbf{0} \quad -\boldsymbol{\delta_q} \quad \mathbf{0}]$$

for plus configurations, and substituting Eqs. 5a, 5b, and 5c, Eq. 4 becomes

$$C_m^B(\phi, \delta_q) = C_m^R(\phi) + C_m^{M_1}(\phi, \delta_q) + C_m^{M_1}\left(\phi + \frac{\pi}{2}, 0\right) \tag{4p}$$

$$+C_m^{M_1}(\phi + \pi, -\delta_q) + C_m^{M_1}(\phi + 3\pi/2, 0)$$

for plus configurations, and

$$C_m^B(\phi, \delta_q) = C_m^R(\phi) + C_m^{M_1}(\phi, \delta_q) + C_m^{M_1}\left(\phi + \frac{\pi}{2}, -\delta_q\right) \tag{4x}$$

$$+C_m^{M_1}(\phi + \pi, -\delta_q) + C_m^{M_1}(\phi + 3\pi/2, \delta_q)$$

for X configurations, indicating that we will actually be pulling from two stripes separated by π rad in bank from the $C_m^{M_1}(\delta_q)$ table and two more separated by π rad in bank from the $C_m^{M_1}(-\delta_q)$ one in the X case.

Next, note that since we are finding the buildup in the Fourier domain, each term in Eqs. 4p and 4x will be found from instances of Eq. 1. For the MAS terms, $T = 2\pi$. When plotting Eq. 1 in the "wind" frame, as the vehicle rolls through a full cycle, the harmonic generated by a pitch deflection should have zero bias (X_0). That is, a flap deflected perpendicular to the pitch plane should produce zero pitch moment. Also, to re-emphasize, we are pulling points separated by π rad in bank to determine a total pitch moment. Thus, we will tune the fundamental frequency amplitude, $|X_1|$, rather than the bias to match the WT totals. Note in Eq. 1 the fundamental amplitude is multiplied by a phase term prior to summing. Substituing $T = 2\pi$, this becomes $\cos(n \cdot \phi + \angle X_n)$ and n = 1 for the fundamental frequency. The roll angle will be replaced with $\phi + \pi/2, \phi + \pi, \ldots$ according to the flap involved. Thus, the assembly at a particular AoA can be viewed as a linear network with inputs $\cos(n \cdot \phi + \angle X_n)$, and gains $|X_n|_m^{M_1}(\delta_q)$ or $|X_n|_m^{M_1}(-\delta_q)$, which will be tuned. For instance,

$$C_m^{M_1}(\phi, \delta_q) = X_0 + \sum_n |X_n|_m^{M_1}(\delta_q) \cdot \cos(n \cdot \phi + \angle X_n) \tag{14}$$

Figure 8 illustrates the buildup path and comparison with WT data.

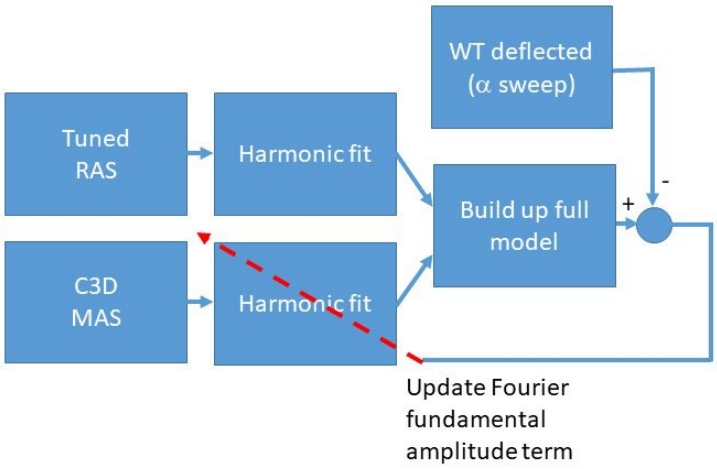

Fig. 8 Tuning MAS terms by backpropagation

At each AoA in $\alpha \in \{0, 2, \ldots, 12\}$ WT data are interpolated to the theoretical AoA. The comparison in Fig. 8 is done twice at each Mach number, pitch deflection, and AoA—once for plus mode, and once for X mode—since plus and X modes share deflections δ_q and $-\delta_q$. We choose to compute $C_m^{M_1}(\phi, \delta_q)$ for all seven AoAs available as a batch, compare, and compute the gradient, so that tuning resembles a steepest descent in vector space rather than simple backpropagation. This results in two residual vectors, $\mathbf{R}_+$ for plus mode and $\mathbf{R}_X$ for X mode. Substituting Eq. 14 into Eq. 4 for the buildup, we can write

$$C_m^B(\phi, \delta_q) = C_m^R(\phi) + \sum_i X_0^{M_i} + \sum_n |X_n|_m^{M_i}(\delta_i) \cdot \cos(n \cdot \phi_i + \angle X_n) \tag{15}$$

Finding the sensitivity of the fundamental harmonic only, the summation in n disappears leaving only the summation in i.

$$C_m^B(\phi, \delta_q) = C_m^R(\phi) + \sum_i X_0^{M_i} + |X_1|_m^{M_i}(\delta_i) \cdot \cos(1 \cdot \phi_i + \angle X_n) \tag{16}$$

Then, realizing that all MAS terms are drawn from the MAS1 model, with adjusted input phase, the total contribution of $|X_1|_m^{M_1}(\delta_i)$ is the second term in the i summation. Thus, the sensitivity of the total pitching moment with respect to the fundamental harmonic amplitude is simply

$$\frac{\partial C_m^B(\phi, \delta_q)}{\partial |X_1|_m^{M_1}(\delta_i)} = \sum_i \cos(1 \cdot \phi_i + \angle X_n) \tag{17}$$

where $\phi_i \in \{\phi, \phi + \frac{\pi}{2}, \phi + \pi, \phi + \ \phi + \frac{3\pi}{2}\}$, and ϕ is the MAS1 aerodynamic bank. If we view Eq. 14 as a single-layer linear network and apply a least-squares criterion

$$E = \frac{p}{2} \sum_p \left(C_m^B(\phi, \delta_q)^p - C_m^{WT}(\phi, \delta_q)^p \right)^2$$

where p indicates a training pair, and WT indicates the WT data, we can write

$$\frac{\partial E}{\partial |X_1|_m^{M_1}(\delta_q)} = \frac{\partial E}{\partial C_m^B(\phi,\delta_q)^p} \cdot \frac{\partial C_m^B(\phi,\delta_q)^p}{\partial |X_1|_m^{M_1}(\delta_q)}$$

where

$$\frac{\partial E}{\partial C_m^B(\phi,\delta_q)^p} = \left(C_m^B(\phi,\delta_q)^p - C_m^{WT}(\phi,\delta_q)^p\right) = \mathbf{R}_i^p$$

Now, recall that for "pitch" configurations, two distinct deflections are used to build up the total. Thus, in plus mode, Flap 1 contributes sensitivity

$$\frac{\partial C_m^B(\phi,\delta_q)}{\partial |X_1|_m^{M_1}(\delta_1)} = \cos(1\cdot\phi_1 + \angle X_n) = \Psi_1$$

while in X mode it becomes

$$\frac{\partial C_m^B(\phi,\delta_q)}{\partial |X_1|_m^{M_1}(\delta_1)} = \cos(1\cdot\phi_1 + \angle X_n) + \cos(1\cdot\phi_1 + \frac{3\pi}{2} + \angle X_n) = \Psi_1 + \Psi_4$$

For the same configurations, Flap 3 is deflected in the opposite direction, so similar expressions are written with $-\delta_1$. Thus, the total sensitivity for a particular deflection can be collected as

$$\frac{\partial E}{\partial |X_1|_m^{M_1}(\delta_q)} = \mathbf{R}_+^p \cdot \Psi_1 + \mathbf{R}_{\mathrm{X}}^p \cdot \Psi_1 + \mathbf{R}_{\mathrm{X}}^p \cdot \Psi_4$$

We employ a simple algorithm where the fundamental amplitudes in the Fourier series model for two deflections $+\delta_q, -\delta_q$ are adjusted at each iteration by

$$|X_1|_m^{M_1}(\delta_q) = |X_1|_m^{M_1}(\delta_q) - \Delta|X_1|_m^{M_1}(\delta_q)$$

and

$$|X_1|_m^{M_1}(-\delta_q) = |X_1|_m^{M_1}(-\delta_q) - \Delta|X_1|_m^{M_1}(-\delta_q)$$

where

$$\Delta|X_1|_m^{M_1}(\delta_q) = \left(\mathbf{R}_+^p \cdot \Psi_1 + \mathbf{R}_{\mathrm{X}}^p \cdot \Psi_1 + \mathbf{R}_{\mathrm{X}}^p \cdot \Psi_4\right)/13$$

The 1/13 learning rate was found to provide good convergence (~15 iterations) without inducing oscillation, and equal weight on each residual resulted lower final residuals.

Figure 9 illustrates the quality of predictions prior to and after training the fundamental Fourier amplitudes. The black diamonds and triangles are the WT total pitch coefficient for each given pitch deflection for plus and X configurations, respectively. The green pluses and X's indicate the model predictions prior to tuning for plus and X configurations, respectively. The red plusses and X's indicate the same predictions after tuning for 15 iterations. After 15 iterations, the sum of 2-norm of the residual vector is reduced on average by 40%. Plus configurations match the training data somewhat better, especially at large AoAs. X configurations are harder to match using this method since points are being drawn from the same Fourier model at a $\pi/2$ phase offset. The residuals are reduced by 38% after just five iterations. The residuals after training are largely due to trade-offs between the two configurations. Note when the initial error for X and plus configurations have opposite polarity, the algorithm is largely unable to eliminate errors. This is especially evident for AoA = 8° and 10° in the examples shown in Fig. 9.

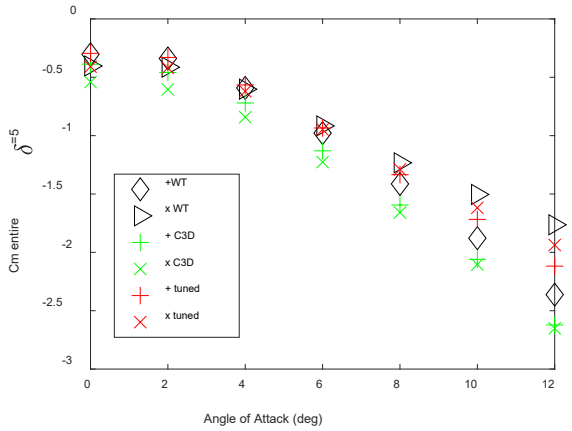

$\delta_q = 5$

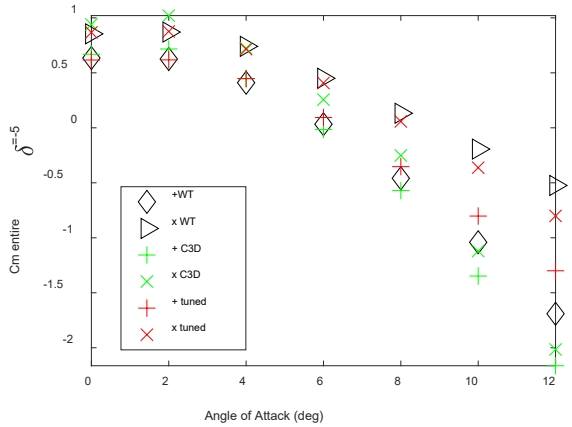

$\delta_q = -5$

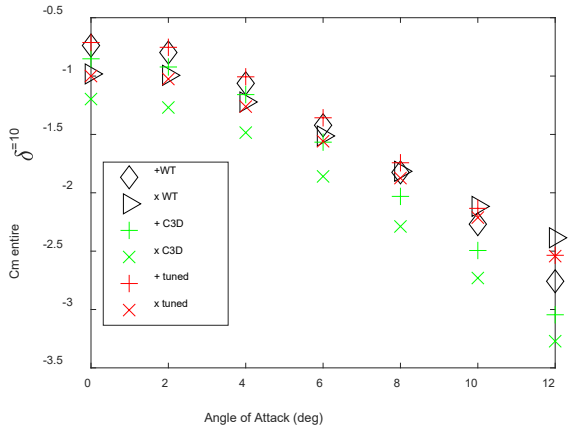

$\delta_q = 10$

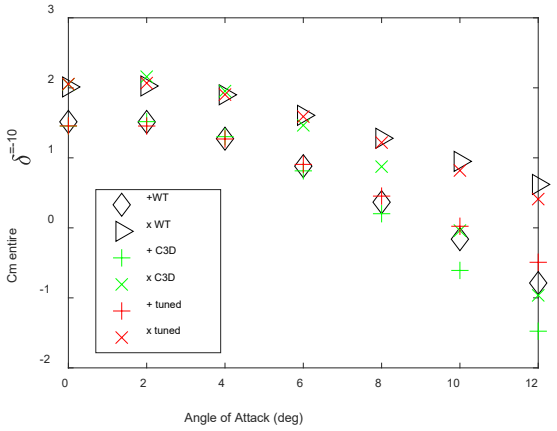

$\delta_q = -10$

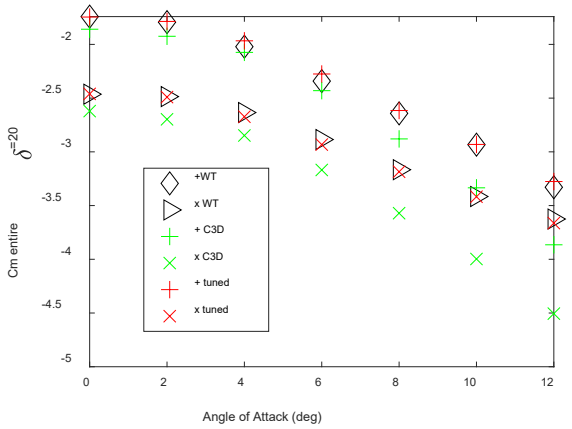

$\delta_q = 20$

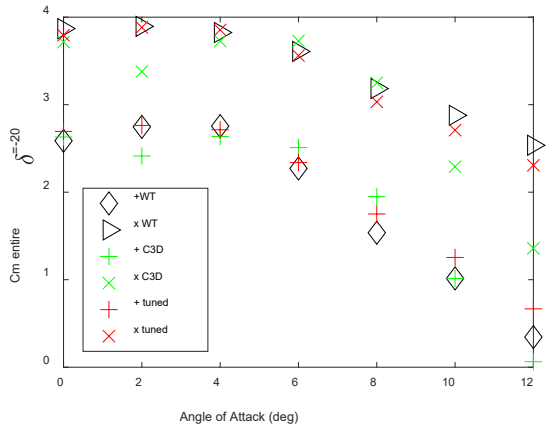

$\delta_q = 20$

Fig. 9 Pitch coefficient matching prior to and after network tuning, Mach = 2.0

5. Polynomial Regression and Build

The final tuned Fourier basis functions

$$((X_0^{M_i}(M,\delta_i,\alpha_j),|X_n|_\vartheta^{M_i}(M,\delta_i,\alpha_j),X_0^R(M,\alpha_j),|X_n|_\vartheta^R(M,\alpha_j))$$

with $\vartheta \in \{A,S,N,l,m,n\}$ are evaluated at $\alpha_j \in \{0°,2°,4°,\dots,20°\}$ using a fine bank grid of $\phi_k \in \{0°,2.8125°,5.625°,\dots,360°\}$. At each bank angle in the grid, the 11 force/moment estimates are collected and a polynomial regression is performed to render a set of polynomial coefficients. For instance, the following normal equation is solved at each Mach M and bank angle ϕ_k to determine a set of entries in the table of polynomial coefficients for RAS pitch moment.

$$\begin{bmatrix} \boldsymbol{s_{0°}^5} & \boldsymbol{s_{0°}^4} & \cdots & \boldsymbol{s_{0°}} & \mathbf{1} \\ \boldsymbol{s_{2°}^5} & \boldsymbol{s_{2°}^4} & \cdots & \boldsymbol{s_{2°}} & \mathbf{1} \\ \vdots & \vdots & \ddots & \vdots & \vdots \\ \boldsymbol{s_{20°}^5} & \boldsymbol{s_{20°}^5} & \cdots & \boldsymbol{s_{20°}} & \mathbf{1} \end{bmatrix} \begin{Bmatrix} C_{m5}^R(M,\phi_k) \\ C_{m4}^R(M,\phi_k) \\ C_{m3}^R(M,\phi_k) \\ \vdots \\ C_{m0}^R(M,\phi_k) \end{Bmatrix} = \begin{Bmatrix} C_m^R(M,\phi_k,0°) \\ C_m^R(M,\phi_k,2°) \\ C_m^R(M,\phi_k,4°) \\ \vdots \\ C_m^R(M,\phi_k,20°) \end{Bmatrix}$$

A similar set of regressions is performed for the MAS terms with the added table dimension of deflection. The aero model (AM) consists of interpolating the resulting tables of polynomial coefficients $C_{\vartheta i}^R(M,\phi), C_{\vartheta i}^M(M,\phi,\delta)$ at the given flight conditions, evaluating the polynomials

$$\begin{aligned} C_\vartheta^R = C_{\vartheta 0}^R(M,\phi) + C_{\vartheta 1}^R(M,\phi)\alpha + C_{\vartheta 2}^R(M,\phi)\alpha^2 + C_{\vartheta 3}^R(M,\phi)\alpha^3 \\ + C_{\vartheta 4}^R(M,\phi)\alpha^4 + C_{\vartheta 5}^R(M,\phi)\alpha^5 \end{aligned} \tag{3}$$

and adding like components as in Eq. 4. The results of this buildup are compared with the original data sources in the next section.

6. Results

The AM described in the previous section was exercised over part of the overall test matrix. Here we show comparisons between the final AM and the data sources to validate our tuning, regressions, and buildup. We present selected cases with zero flap deflections, as these were the most densely populated across data sources. An alternative model was formed to compare our method with a basic kriging method[4] (KRIGE). Kriging was used by finding a Gauss process regression model of differences $\hat{\beta}_\vartheta^{WT}$ between the CART3D data and WT data using points in the WT database. True values of β_ϑ^{WT} are found where data exist from both sources.

$$\beta_{\vartheta}^{WT} = C_{\vartheta}^{WT} - C_{\vartheta}^{C3D} \tag{18}$$

The Gauss process regression model is found from these points and used to predict $\hat{\beta}_{\vartheta}^{WT}$ for the entire test matrix. A second kriging model was also found from the differences $\hat{\beta}^{NS}$ between Navier–Stokes predictions and Cart3D. The kriging models are then used to move the Cart3D surface closer to the truth by forming two averaged databases by

$$C_{\vartheta}^{*} = C_{\vartheta}^{C3D} + a \cdot \hat{\beta}^{WT} + b \cdot \hat{\beta}^{NS} \tag{19}$$

where $a + b = 1$. The first uses $a = 1$ and $b = 0$ and is labeled "wtKRIGE" in the plots. The second sought to combine the traits of all data sources and used $a = \frac{1}{2} + \frac{\sqrt{5}}{2} - 1$ and $b = 1 - a$. This case is labeled "bthKRIGE" in the plots. These data are then used to find a Fourier basis for RAS terms in similar fashion as our model. Thus, it benefits from the symmetry imposed by Fourier.

Figure 10 shows the side moment for a range of Mach numbers at 22.5° of roll angle. This attitude was selected because symmetry should cause a zero side moment at 0° and 45°. WT data were available at this attitude for 0°, 6°, and 12° AoA since roll sweeps were performed at these values. In Fig. 10a, four of the six models overlap at exactly zero. This stems from the symmetry of the 3-D model imported into each CFD code. It is expected to exhibit zero moments at zero AoA (i.e., no "trim" moments). WT data show some slight deviations from theoretical perfection. Cart3D predicts non-zero trims at a few Mach numbers, most likely due to incomplete convergence. The AM is set to ignore the WT values when previous methods predict a zero force or moment—and it exhibits that behavior here. Figure 10 (top right and bottom left) show some consequences of the sequential tuning. Trends are not remembered from AoA to AoA or from Mach to Mach, but memory of previous data sources exists at a particular Mach and AoA. Fig. 10, bottom left, is a good example of this. The algorithm starts with the C3D curve. It is tuned to the CFD++ data ("NS"), which would draw it slightly lower.

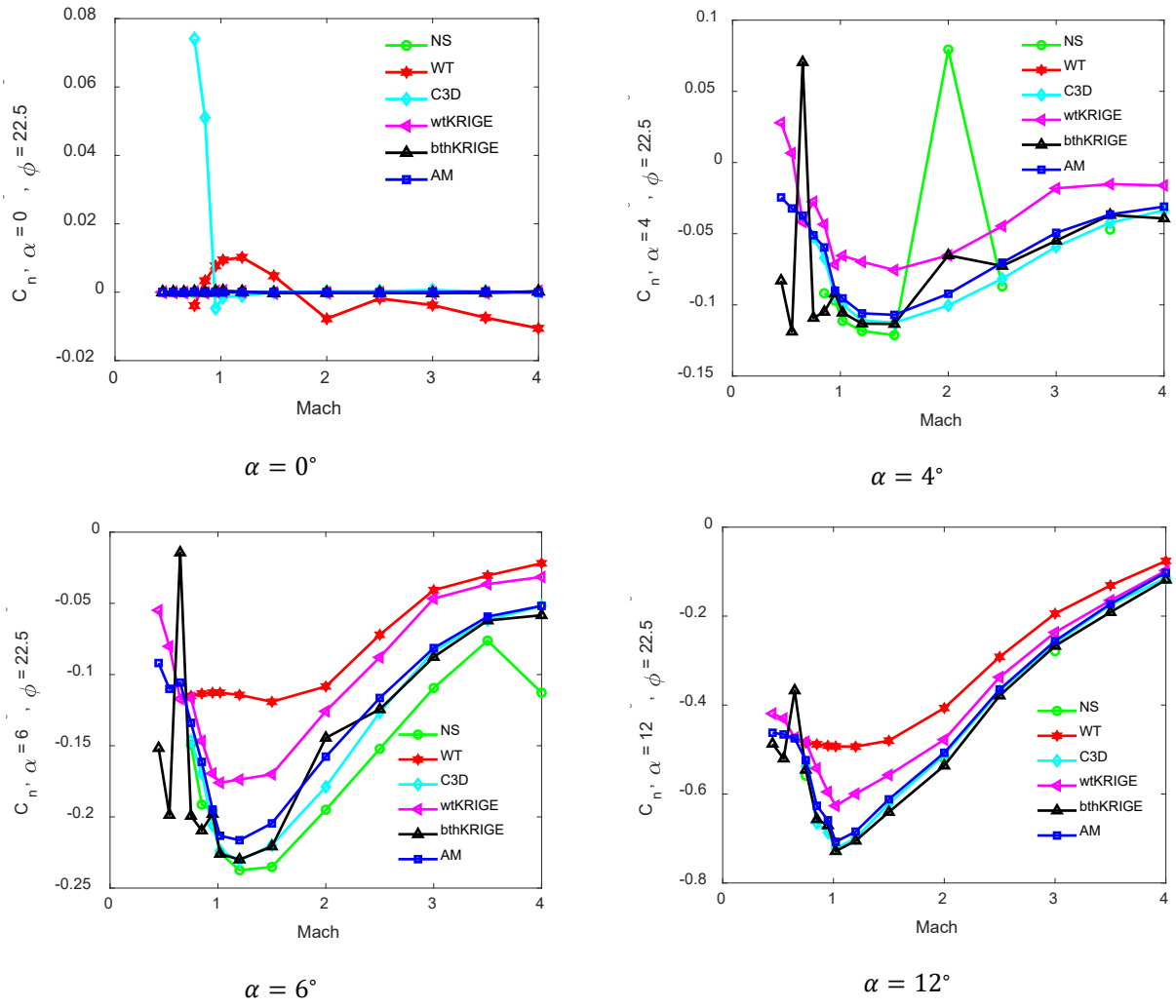

Fig. 10 Side-moment coefficient comparison for all data sources, plus mode, Mach = 2.0, roll angle = 22.5°

In the final step, the AM curve is tuned to the "WT". However, due to limited iterations, the model moves only slightly toward the WT data, therefore respecting the previous data sources. Keep in mind the y-axis scaling in each of these plots. Since residuals are quite small to begin with, training to the WT data is not very aggressive. Likewise, the kriging model resembles the Cart3D data for the points shown. WT data for this bank angle only exists at 0°, 6°, and 12° AoA. Apparently, the kriging model has difficulty interpolating the other points from neighboring bank angles, something our algorithm is better at because the harmonic bases are introduced earlier in the process.

Figure 11 shows the pitch coefficient training for $\alpha = 2°, 4°, 6°, 8°, 10°$, and 12°. Cart3D predictions are shown in cyan, CFD++ in green, WT in red, and AM in blue. Note in each case C_m gets more strongly negative as each subsequent data source is used: the curve moves downward. However, the previous data sources are

not completely supplanted since the final AM curve is slightly higher than the WT curve. The three data source curves and final model all morph to a common shape as AoA increases. For small AoA, the AM curve conforms to the WT data. Keep in mind that no memory exists from AoA to AoA; however, in the final model, distinct points in AoA are tied together through polynomial regression.

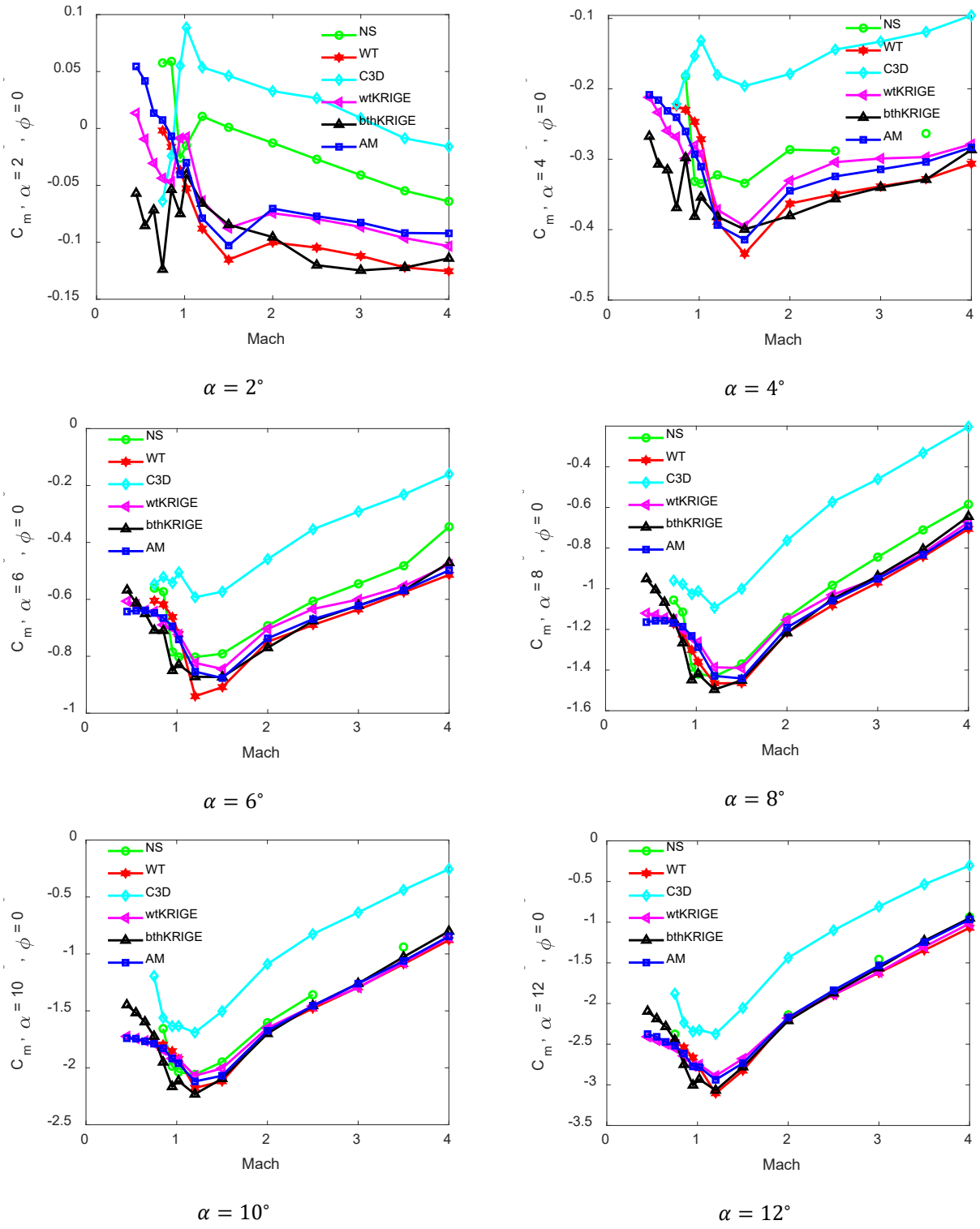

Fig. 11 Pitch coefficient comparison for all data sources, Mach = 2.0, roll angle = 0°

Figure 12 shows the results for side force. Again, a roll angle of 22.5° was selected, because symmetry should produce a zero side force at 0° and 45° roll angles, and the model is able to ignore the non-zero trims from the WT and Cart3D. Side-force

predictions from the AM exceed the three sources (C3D, NS, and WT) for nearly all cases shown. What is not evident in these plots is that this is caused by the harmonic interpolation and polynomial regression, which happen after all data sources are considered. In other words, the Fourier series is truncated at three harmonics, so it will not exactly match the training at every roll angle (overfitting), but it will enforce the symmetry and null points expected from the projectile geometry. Thus, some amplitudes in the final model will exceed the data sources and others will be reduced. Second, the polynomial fitting induces a smoothing across AoAs. This can prove adverse if the force/moment of interest does not monotonically increase in magnitude with increased AoA. These effects combine to cause the final model to "forget" some of the finer details in the data sources.

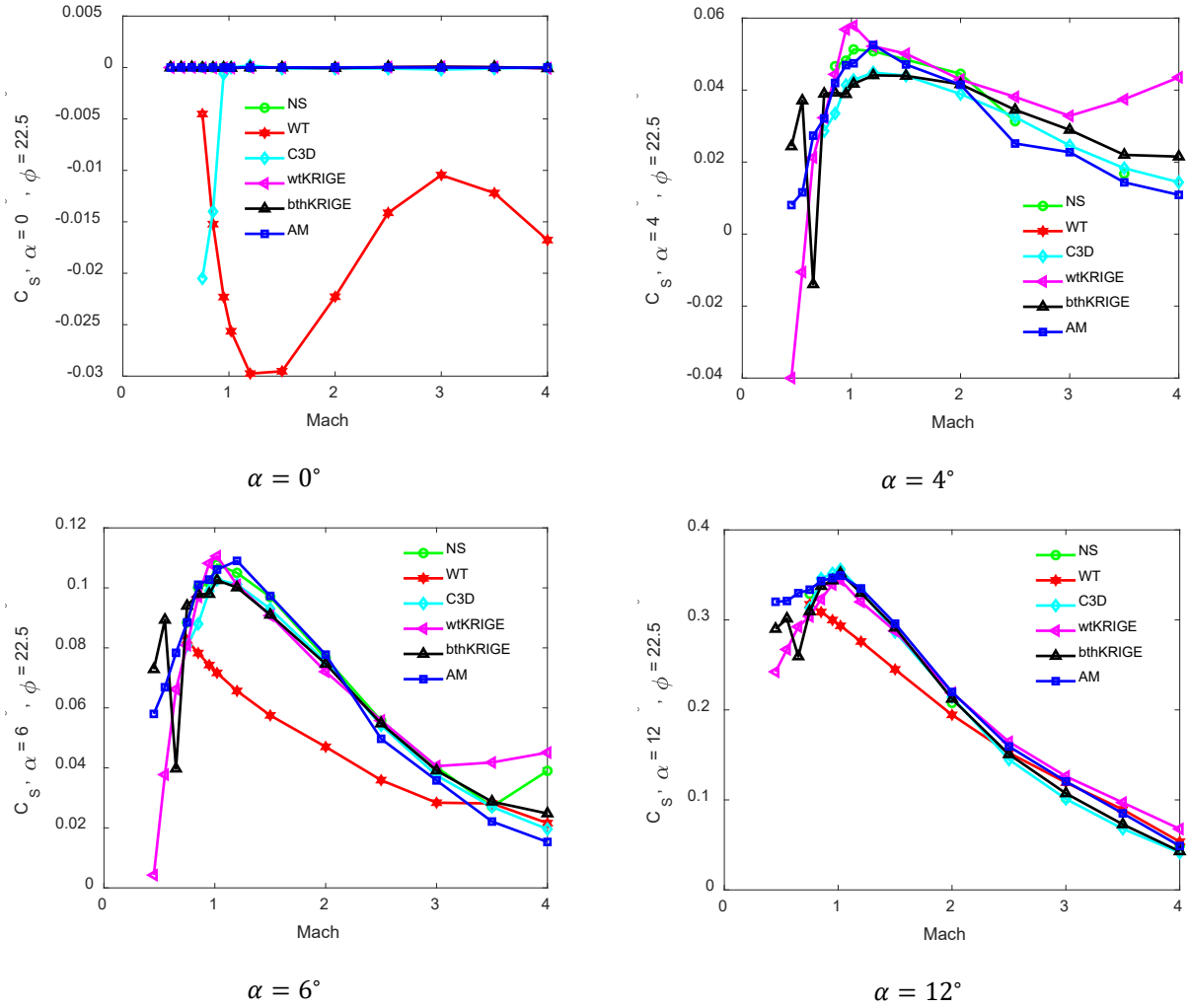

Fig. 12 Side-force coefficient comparison for all data sources, plus mode, Mach = 2.0, roll angle 22.5°

Figure 13 shows a sample result for normal force at 22.5° of bank. Once again, the AM predicts no trim force at zero AoA. Figure 13c shows another good example of the influence of subsequent data sources. Starting from the cyan curve (C3D), training pushes the model up near the green curve (NS), then down toward the red curve (WT). Since the residuals between NS and WT are small, some of the trends from NS remain in the final model. As AoA is further increased, all data sources converge to a common shape. The AM provides a good balance at $\alpha = 12°$ among all three data sources, with high Mach number predictions finding a happy medium between CFD++ (green) and WT (red).

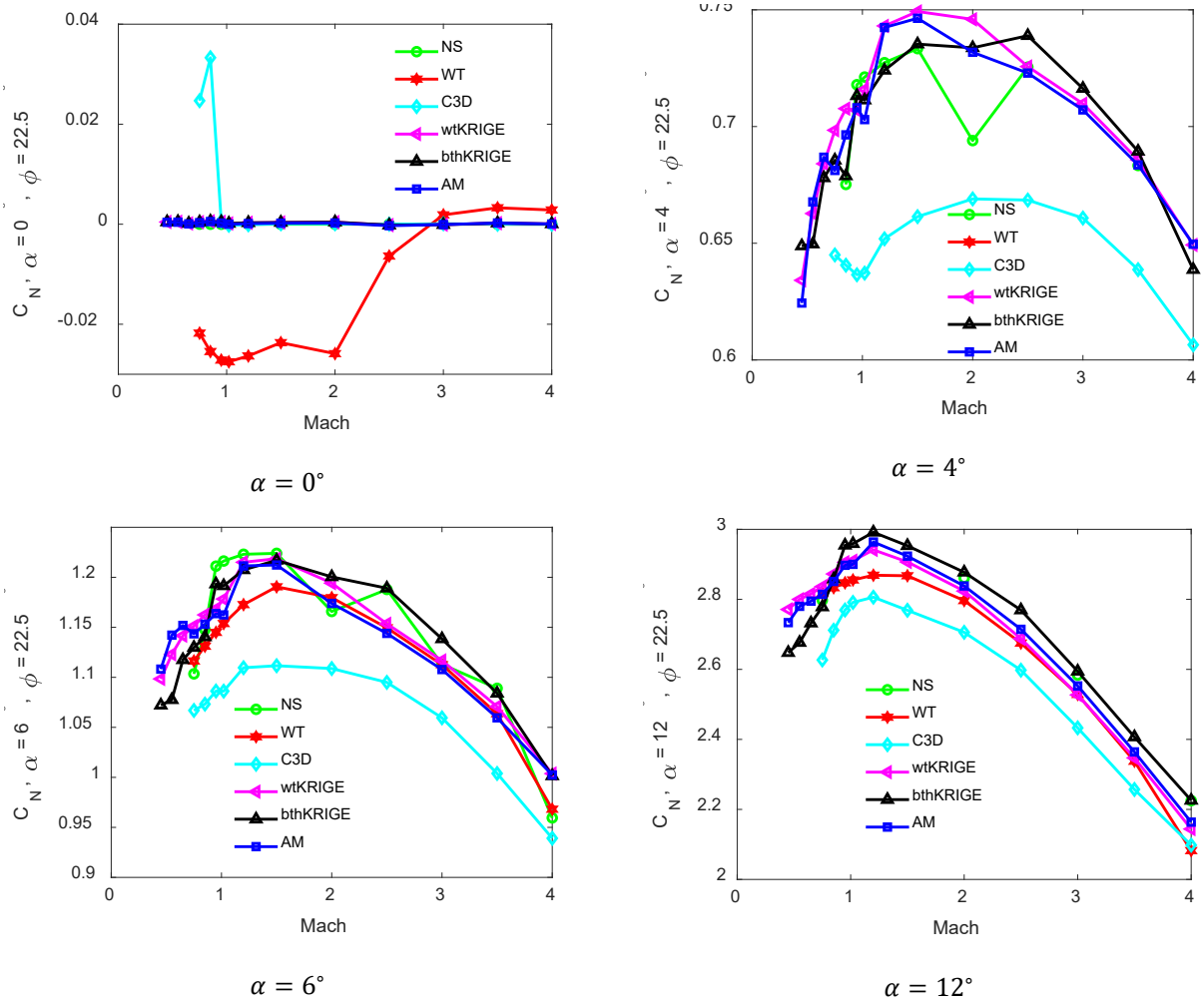

Fig. 13 Normal force coefficient comparison for all data sources, plus mode, Mach = 2.0, roll angle = 22.5°

7. Conclusion

A novel approach to combining aerodynamic data sources for roll-dependent aerodynamics has been developed and tested. By finding and training a set of basis functions, sparse but accurate data sources were used to refine the model accuracy while preserving trends predicted by low-fidelity computation methods. The final model averages all data sources and exhibits symmetry and null points expected from the airframe geometry. By using harmonic basis functions, our method informs the model of the airframe geometry, unlike kriging models, which are solely based on available data. Our method balanced contributions from all data sources and converged much faster than the kriging approach.

8. References

1. Bryson JT, Vasile JD, Bruenwald BC, Saju J, Fresconi F. Modeling and flight dynamics of a projectile with nonlinear, roll-dependent aerodynamics. Proceedings of the AIAA SciTech Forum; 2021 Jan.

2. Vasile J, Bryson J, Sahu J, Paul J, Gruenwald B. Aerodynamic dataset cohort of a long-range projectile. DEVCOM Army Research Laboratory; 2020 Aug. Report No.: ARL-TR-9019.

3. Vasile JD, Sahu J. Roll orientation–dependent aerodynamics of a long-range projectile. DEVCOM Army Research Laboratory; Aug 2020. Report No.: ARL-TR-9017.

4. Ghoreyshi M, Badcock KJ, Woodgate MA. Integration of multi-fidelity methods for generating an aerodynamic model for flight simulation. Proceedings of the 46th AIAA Aerospace Sciences Meeting and Exhibit; 2008 Jan.

5. Khatamsaz D, Allaire DL. A comparison of reification and cokriging for sequential multi-information source fusion. Proceedings of the AIAA SciTech Forum; 2021 Jan.

6. Burt HB, Millidere M, Gomec FS, Ugur O. Multi-fidelity aerodynamic dataset generation of a fighter aircraft. Proceedings of the AIAA SciTech Forum; 2021 Jan.

7. Burchett BT, Paul J, Vasile JD. Bryson JT. A high-fidelity roll-dependent aerodynamic model for a long-range high-speed missile. DEVCOM Army Research Laboratory; in preparation.

8. Pokela R, Kumar R, Vasile J. Experimental and computational aerodynamic characterization of a generic high-speed projectile configuration. Proceedings of the AIAA Aviation Forum; 2021 Aug.

List of Symbols, Abbreviations, and Acronyms

3-D	three-dimensional
6DOF	6 degrees of freedom
Al	aileron
AM	aero model
AoA	angle of attack
C3D	Cart3D Euler Computation Fluid Dynamic code
CAD	computer-aided design
CFD	computation fluid dynamics
DATCOM	United States Air Force Stability and Control Digital
El	elevator
LTV	Laboratory Technology Vehicle
MAS	moveable aerodynamic surface
NaN	not a number
NASA	National Aeronautics and Space Administration
NS	Navier–Stokes
RANS	Reynolds-averaged Navier–Stokes
RAS	rigid aerodynamic surface
WT	wind tunnel
$\lvert X_n \rvert \angle X_n$	magnitude/phase of polar Fourier harmonic *n*
T	period of harmonic function [rad]
$\mathbf{I}$	identity matrix
a_n, b_n	Cartesian Fourier amplitudes
i	$= \sqrt{-1}$
M	Mach number
$\mathbf{\Phi}$	Matrix of harmonic basis functions
ϑ	placeholder, $\vartheta \in \{A, S, N, l, m, n\}$

$\mathbf{R}$	Rotation Matrix
α	angle of attack [deg]
δ	flap deflection [deg]
$f(.)$	function to be approximated
D	projectile diameter [m]
C_A	axial force coefficient
C_S	side force coefficient
C_N	normal force coefficient
C_l	roll moment coefficient
C_m	pitch moment coefficient
C_n	yaw moment coefficient
Subscript	
n	harmonic number
Superscript	
T	matrix transpose
L	placeholder, $L \in \{R, M_1, M_2, M_3, M_4\}$
R	rigid aerodynamic surface
M_j	moveable aerodynamic surface j
B	body frame
WT	wind tunnel frame
N	normal force component
S	side force component

1 (PDF)	DEFENSE TECHNICAL INFORMATION CTR DTIC OCA
1 (PDF)	DEVCOM ARL FCDD RLD DCI TECH LIB
1 (PDF)	DEVCOM AC RDAR MEM A M DUCA
3 (PDF)	DEVCOM AVMC FCDD AMS MMA J DOYLE C ROSEMA M MCDANIEL
1 (PDF)	JHU/APL A NEDUNGADI
1 (PDF)	SNL C SMITH
1 (PDF)	FSU R KUMAR
28 (PDF)	DEVCOM ARL FCDD RLW J ZABINSKI FCDD RLW A F FRESCONI FCDD RLD S SILTON FCDD RLW TF R SUMMERS FCDD RLW W W OBERLE P PEREGINO T SHEPPARD FCDD RLW WA N TRIVEDI E BYRD FCDD RLW WB J SADLER FCDD RLW WC A WILLIAMS M NUSCA A MCBAIN M MINNICINO FCDD RLW WD L D FAIRFAX V BHAGWANDIN B GRUENWALD I CELMINS J SAHU B BURCHETT J VASILE J BRYSON L STROHM J DESPIRITO FCDD RLW WE M ILG B TOPPER D EVERSON T BROWN